Parameter Estimation for the OJ287 Binary Black Hole System

Brian Sheridan
18373446

April 22, 2022

Supervised by Dr. Vojtěch Witzany and Dr. Sarp Akçay

This thesis is submitted to University College Dublin in partial fulfilment of the requirements for the degree of BSc in Theoretical Physics

School of Physics
University College Dublin
An Coláiste Ollscoile, Baile Átha Cliath

Abstract

The OJ 287 system is a celestial object which exhibits quasi-periodic variations in its light intensity over an approximately 12 year period and a longer 60 year period. Previous models of OJ 287 which predict the most accurate light outburst times are of a supermassive binary black hole. A primary black hole is surrounded by an accretion disk and is orbited by a secondary black hole of much less mass. The outbursts are assumed to correspond to the secondary black hole crossing the accretion disk. This thesis implements a model for the OJ 287 system to predict outburst times. The parameter space of the system is scanned by making a least squares fit with the observed outbursts for each combination of parameters in order to find the optimum solution with predictions closest to observations. The parameters which provide the best fit are a system mass of $M = 3 \times 10^{10}\,\mathrm{M}_{\odot}$, a black hole spin of $a = 0.1$ in units of the black hole mass, an orbital semi-latus rectum of $p = 34$ in units of the black hole mass, an eccentricity of $e = 0.8$ and a minimum orbital polar angle of $\theta_{\mathrm{min}} = \pi/6$ radians. The average magnitude of the deviation of the predictions from observations is 8.64 years, suggesting a moderate fit with observations.

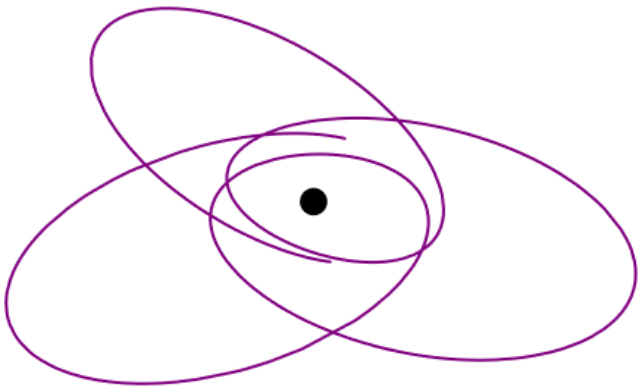

An example of a geodesic in Kerr space-time around a rotating black hole.

Acknowledgements

I would like to thank my two supervisors Vojtěch Witzany and Sarp Akçay for their patience, insight and guidance throughout this project. It was a pleasure to work with them throughout the year and I thank them for all I learned from them.

I would also like to thank the UCD School of Physics and the School of Mathematics and Statistics for the support to pursue a final year research project, fellow student Hugh Kelly for the helpful insight and discussions about Kerr geodesics throughout the academic year and my mother for all her support while writing this thesis.

Declaration of Authorship

I declare that all material in this project is my own work, except where there is clear acknowledgement and appropriate reference to the work of others.

Contents

List of Figures

List of Tables

1 Introduction

"Sire, there is no royal road to geometry." - Euclid of Alexandria.

The collective astronomical eye of society has wandered the night sky for millennia. From initial curiosities regarding the motion of the planets, the "wanderers" of the night sky, our capacity to observe celestial phenomena has grown over time, extending our observational eye far beyond our own solar system and the Milky Way galaxy. Observing such a plethora of objects in the night sky all with differing features implores us to construct explanations for what we see. One such interesting celestial object we observe is the OJ 287 system. This system lies along the ecliptic, which is the plane of the Earth's orbit around the Sun. It is the section of the night sky for which most of the planets can be observed and thus has been a region of historical astronomical interest. The current redshift value for OJ 287 of $z = 0.304$ [3] places the object at approximately 3.5 billion light years away from Earth. However, due to its fortunate location along the ecliptic, observations of the OJ 287 system have existed for over a hundred years, even being seen on photographic plates as far back as 1887 [4]. From these extended observations we have observed that the light curve of OJ 287, which describes the apparent magnitude of the system as viewed from Earth, exhibits quasi-periodic bursts of intensity approximately every 12 years with a longer quasi-periodic variation of about 60 years, as seen in Figure 1 and Table 1. This unusual double quasi-periodic behaviour, being one of the first confirmed cases of an extragalactic object with a periodicity other than variable stars [5], suggests an interesting mechanism behind the light variations of the OJ 287 system and implores us to construct a theoretical model to describe its behaviour. It is the goal of this thesis to build a simple model for the OJ 287 system in order to predict the bursts of light intensity and to validate the model by comparing it to observations.

1.1 Previous Models of OJ 287

The variations of the emitted light intensity, and thus the apparent magnitude, pose an interesting question. What exactly is the system OJ 287 and what is powering the periodic light variations? Previous efforts have attempted to construct a model of the system to reproduce the historical light curve and answer this question. Begelman, Blanford and Rees assumed a binary black hole system, although stipulating that the accretion disk surrounding the system precess [6]. The effect of this precession would be to control the outburst intensity and Doppler shift of an emitted jet. This model, however, typically predicts periodicities on the order of a few hundred years, in disagreement with observations of approximately 12 years. J. I. Katz suggested that the periodicity is caused by a precessing relativistic beam emanating from OJ 287 which sweeps across our line of sight [5]. In this model, there exists not only the relativistic jet, but also an accretion disk that is inclined to line of sight of Earth observations which precess around the black hole and also exhibits a "nodding" behaviour. These previous suggestions, yielding inaccurate predictions, leave space to suggest another model for the system; that of a supermassive binary black hole system, proposed by Sillanpaa and with model improvements by

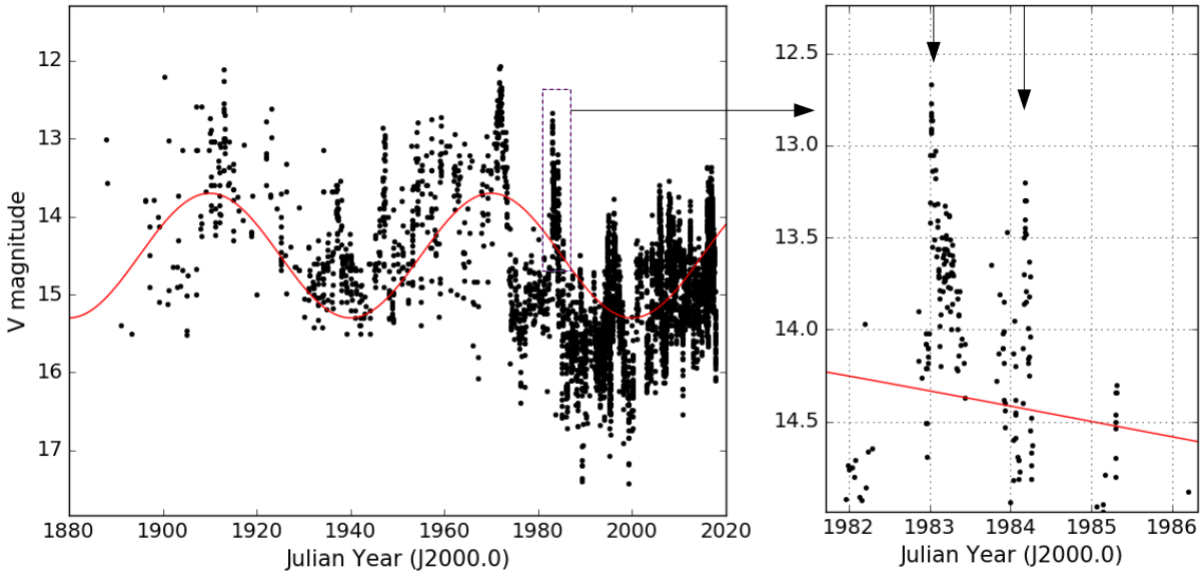

Figure 1: The historical measurements of the light intensity from the OJ 287 system. The quasi-periodic peaks of approximately 12 years are apparent over longer time scales. [1]

Lehto and Valtonen [7]. The idea is that a primary black hole surrounded by an accretion disk is orbited by a secondary black hole of a much smaller mass. The peaks of the light intensity correspond to the crossings of the secondary black hole past the accretion disk, in which its interaction causes a burst of light. The longer period is related to the precession of the orbit of the secondary around the primary. Previous efforts to predict the historical light curve using this model have been quite successful [4]. The model by Lehto and Valtonen has even predicted outbursts following the 2015 outburst to within hours [8] [9]. The precision of these predictions provide excellent grounds for validating the model of a supermassive binary black hole, and so OJ 287 represents one of the first tangible candidate for a supermassive binary black hole system at the centre of a galaxy [1]. Supermassive black holes at the centre of galaxies are typically surrounded by accretion disks, which provide luminosity to the black hole system from the conversion of viscous, thermal and gravitational energies to electromagnetic radiation. These galactic nuclei which shine as brightly as, or brighter than, the host galaxy are called active galactic nuclei (AGN). These active galactic nuclei often emit jets of radiation and relativistic particles, and when this sweeping jet points to our line of sight from Earth the active galactic nucleus is classified as a blazar [10].

1.2 Supermassive Black Hole Binary

The goal of this thesis is to apply a model for a supermassive binary black hole system using the Theory of General Relativity and to implement it numerically in order to estimate parameters of the binary black hole system. Due to the success of previous models, the outbursts will be modelled as the interaction of the secondary black hole with the accretion disk around the primary. A scan of parameter space will be made in order to estimate the parameters of the system. The predictions of the historical light curve will be made for each set of system parameters until the set is found which matched the historical light curve the closest.

Observed Outburst Times (Julian Year)
1912.980
1947.283
1957.095
1972.935
1982.964
1984.125
1995.841
2005.745
2007.6915
2015.875

Table 1: The outburst times of 10 well recorded observations of the OJ 287 system. The times are taken as point values and are in the form of the Julian year [1]. Note that since 2015 there has been another recorded outburst in 2020 [2].

The orbital model used approximates the secondary black hole as a test particle and treats its trajectory around the primary black hole as a geodesic. It is treated as a zeroth order approximation to the true equations of motion of the system, which would take the mass of the secondary black hole into account. This approach is justified since it is assumed that the mass of the secondary black hole is much smaller than that of the first. Previous investigations of the OJ 287 system place the ratio of the masses to be a little less than 1/120 [4]. In order to create and numerically implement a model of the supermassive binary black hole system, we require a robust and accurate theory to model the gravitational effects of the system and to model the trajectory of the geodesic. Newtonian physics has long since provided an accurate model for systems of low mass, however it is only applicable to weak gravitational fields and low velocities. These criteria are satisfied in bound systems for which the dimensionless potential Φ/c^2 is small everywhere. For environments where this quantity is not small, such as the space-times surrounding a black hole, we require a more powerful theory of gravity to deal with these strong fields, namely The Theory of General Relativity.

2 General Relativity

"Space-time tells matter how to move; matter tells space-time how to curve."

- John Wheeler.

The inverse-square force law of gravitation proposed by Isaac Newton in his ground-breaking work *Principia* in 1687 provided an excellent model for the gravitational interactions and forces between masses, correctly predicting a number of phenomena such as the period of Halley's Comet [11] and the discovery of the planet Neptune [12]. However limitations of the model became apparent after some time. By the beginning of the 20th century, astronomers had noticed a discrepancy between the observed positions of Mercury in the night sky and positions predicted by Newtonian mechanics, to which a resolution to this problem was only achieved with the development of the General Theory of Relativity by Albert Einstein

in 1915 [13]. The theory correctly predicted the precession of Mercury's orbit around the sun, demonstrating its accuracy to model gravity around large masses, such as Mercury and its close proximity to the Sun.

In order to arrive at his theory, Einstein first considered a long-standing empirical fact about the mass of an object. The equation of motion of an object in a gravitational field is given as

$$\frac{d^2\vec{x}}{dt^2} = -\frac{m_G}{m_I}\vec{\nabla}\Phi\,, \tag{1}$$

where m_G and m_I are the gravitational and inertial masses of an object, respectively, and the gravitational potential Φ is determined by Poisson's equation $\nabla^2\Phi = 4\pi G\rho$. Experiments show that the ratio m_G/m_I is the same for any object, and therefore by choosing a particular set of units, can be set to unity, meaning that the object's motion in a gravitational field is independent of the nature of the object [13]. This result led Einstein to formulate the *Equivalence Principle*, stating that a freely-moving reference frame resembles a Cartesian inertial frame and the laws of physics are the same as Special Relativity. The insight from Einstein suggests that gravity is no longer a conventional force, rather the manifestation of the curvature of space-time; the curvature being induced by the presence of matter. This revelation suggests that we are no longer able to perform calculations in a flat space-time such as that of Newtonian physics or Special Relativity, but rather must consider a curved space-time.

The curvature of space-time by gravity requires the construction of a curved space-time manifold. In general, a manifold is a topological space that is locally Euclidean at any point. The particular manifold in General Relativity is the Riemannian Manifold. This is a real and smooth manifold characterised by the general form of the infinitesimal line element,

$$ds^2 = g_{\mu\nu}dx^\mu dx^\nu\,, \tag{2}$$

where the Einstein summation convention is used.

Among the many interesting topics in General Relativity is the trajectory of a body through space-time. In particular, a *geodesic* is the curve which extremises the length of the path between two points. It is the path which extremises the action taken and thus satisfies the Euler-Lagrange equations. This path can be interpreted as the trajectory through space-time that a freely falling test-mass particle would take. The general form of the equation governing the geodesic trajectory is

$$\frac{d^2x^\alpha}{du^2} + \Gamma^\alpha_{\beta\gamma}\frac{dx^\beta}{du}\frac{dx^\gamma}{du} = \lambda(u)\frac{dx^\alpha}{du}\,, \tag{3}$$

where u an *affine parameter*. Considering the tangent vector $\mathbf{t}$ to the curve $x^a(u)$, parameterised by u, at every point in

space such that

$$|\mathbf{t}| = |g_{\mu\nu} t^\mu t^\nu|^{1/2} = \frac{|g_{\mu\nu} dx^\mu dx^\nu|^{1/2}}{du} = \left| \frac{ds}{du} \right| , \tag{4}$$

describes the length of the tangent vector along the curve, an affine parameter is any $u = as + b$ with $a \neq 0$ such that the length of the tangent vector is constant as it is parallel transported along the curve. The effect of the affine parameter on Equation (3) is that it reduces $\lambda(u)$ to zero, for affine u. A commonly used affine parameter is the *proper time* τ, which is the time measured in a frame of reference moving along with the trajectory of the body. This reduces the geodesic equations to be

$$\frac{d^2 x^\alpha}{d\tau^2} + \Gamma^\alpha_{\beta\gamma} \frac{dx^\beta}{d\tau} \frac{dx^\gamma}{d\tau} = 0 . \tag{5}$$

The values $\Gamma^\alpha_{\beta\gamma}$ are known as the *affine connection*, or the *Christoffel symbols of the second kind*, and quantify the change of the basis vectors as the coordinates are varied in the manifold, namely

$$\frac{\partial \mathbf{e}_\beta}{\partial x^\gamma} = \Gamma^\alpha_{\beta\gamma} \mathbf{e}_\alpha . \tag{6}$$

Since these Christoffel symbols relate the basis vectors to the changes in those basis vectors in space-time, they contain all the information about the curvature of that space-time. More conveniently for calculations, these quantities can be defined in terms of the metric tensor of the space-time as

$$\Gamma^\alpha_{\beta\gamma} = \frac{1}{2} g^{\alpha\sigma} (\partial_\beta g_{\gamma\sigma} + \partial_\gamma g_{\sigma\beta} - \partial_\sigma g_{\beta\gamma}) . \tag{7}$$

We can therefore see that solutions to the geodesic equations rely on the space-time metric, along with suitably defined space-time coordinates. The solutions to the space-time metric are determined by Einstein's Field Equations. These are the central equations of general relativity, describing the relationship between the curvature of space-time and the energy presence of matter, given as

$$G^{\mu\nu} = R^{\mu\nu} - \frac{1}{2} R g^{\mu\nu} = \frac{8\pi G}{c^4} T^{\mu\nu} , \tag{8}$$

where $G^{\mu\nu}$ is the Einstein Tensor, $R^{\mu\nu}$ is the Ricci Tensor and is given by the contraction over the Riemann Tensor, R is the Ricci Scalar and is given as the contraction over the Ricci Tensor, and $T^{\mu\nu}$ is the Energy-Momentum Tensor, or the Stress-Energy Tensor, which specifies the source of the space-time curvature due to the presence of matter.

This equation can be used to obtain the form of the space-time metric $g_{\mu\nu}$ for a given space-time. From the vast array of imaginable space-times, the *no hair theorem* [14] for black holes greatly reduces the types of space-times we need to consider in our pursuit to model the OJ 287 system. This theorem states that black holes can be characterised by only three macroscopic parameters, the mass M, the angular momentum J and the net charge Q. The different types of black holes from these parameter combinations is given in Table 2. There are also more exotic space-time metrics, such as the

Taub-NUT space-time [15], although these are not included in the table.

Black Hole Categorisations		
	Uncharged ($Q = 0$)	*Charged* ($Q \neq 0$)
Non-Rotating ($J = 0$)	Schwarzschild	Reissner-Nordström
Rotating ($J \neq 0$)	Kerr	Kerr-Newman

Table 2: The different classifications of black holes.

If we consider a charged black hole, the net charge would attract particles of opposite charge toward the black hole, from sources such as an accretion disk around the black hole. By conservation of charge, the opposite charges should cancel when the particle enters the black hole. Therefore a charged black hole should become uncharged over time when interacting with matter in the universe. We are then led to consider two famous results for the space-time metric around black holes, the Schwarzschild and the Kerr solutions, for when the black hole is non-rotating and rotating, respectively.

2.1 Schwarzschild Space Time

"As you see, the war treated me kindly enough, in spite of the heavy gunfire, to allow me to get away from it all and take this walk in the land of your ideas."- Karl Schwarzschild in a letter to Albert Einstein.

The first solution to the Einstein Field equations was discovered in 1915 by Karl Schwarzschild while fighting on the front lines of World War I [16]. By considering a spherically symmetric, non-rotating body he was able to derive the form of the generated space-time metric, given in Boyer-Lindquist coordinates as

$$ds^2 = -\left(1 - \frac{2GM}{c^2 r}\right) c^2 dt^2 + \left(1 - \frac{2GM}{c^2 r}\right)^{-1} dr^2 + r^2(d\theta^2 + \sin^2\theta d\phi^2)\,. \tag{9}$$

The geodesic equations can be derived with the Lagrangian approach, by using the Euler-Lagrange equations of motion

$$\mathcal{L} = \frac{1}{2} g_{\mu\nu} \dot{x}^\mu \dot{x}^\nu\,, \tag{10}$$

$$\frac{d}{d\tau}\left(\frac{\partial \mathcal{L}}{\partial \dot{x}^\mu}\right) - \frac{\partial \mathcal{L}}{\partial x^\mu} = 0\,. \tag{11}$$

Using Equation (10), the resulting Lagrangian for the Schwarzschild space-time is given as

$$\mathcal{L} = \frac{1}{2}\left(-\left(1 - \frac{2GM}{c^2 r}\right) c^2 \dot{t} + \left(1 - \frac{2GM}{c^2 r}\right)^{-1} \dot{r}^2 + r^2\dot{\theta}^2 + r^2 \sin^2\theta \dot{\phi}^2\right)\,. \tag{12}$$

Substituting this Lagrangian into Equation (11) gives the geodesic equations for the Schwarzschild space-time

$$E = \left(1 - \frac{2GM}{c^2 r}\right)\dot{t}\,, \tag{13}$$

$$L = \dot{\phi}\, r^2 \sin^2\theta\,, \tag{14}$$

$$0 = \ddot{\theta} + \frac{2\dot{r}\dot{\theta}}{r^2} - \dot{\phi}^2 \sin\theta\cos\theta\,, \tag{15}$$

$$0 = \ddot{r}\left(1 - \frac{2GM}{c^2 r}\right)^{-1} - \dot{r}^2\left(\frac{GM}{c^2 r^2}\right)\left(1 - \frac{2GM}{c^2 r}\right)^{-2} + \frac{GM\dot{t}^2}{r^2} - r(\dot{\theta}^2 + \dot{\phi}^2\sin^2\theta)\,, \tag{16}$$

where an over dot denotes the derivative with respect to the proper time τ. We see two conserved quantities, the energy E per unit mass and the angular momentum L per unit mass, which reduce the t and ϕ equations to first order ordinary differential equations. Positive values of the energy are taken for particles moving forward in time.

We see immediately that $\theta = \pi/2$ satisfies Equation (15). Since the Schwarzschild black hole is not rotating the geodesic trajectory is confined to a plane. Without loss of generality, we can take this plane to be the equatorial plane of the black hole, which justifies our solution to take $\theta = \pi/2$. This reduces the equations to the following form

$$\dot{t} = E\left(1 - \frac{2GM}{c^2 r}\right)^{-1}\,, \tag{17}$$

$$\dot{\phi} = \frac{L}{r^2}\,, \tag{18}$$

$$\theta = \pi/2\,, \tag{19}$$

$$\ddot{r} = \left(1 - \frac{2GM}{c^2 r}\right)\frac{L^2}{r^3} - \left(\frac{GM}{c^2 r^2}\right)\left(1 - \frac{2GM}{c^2 r}\right)^{-1}(c^2E^2 - \dot{r}^2)\,. \tag{20}$$

This results in the general solution for the Schwarzschild geodesics. However, in practice, the second order radial solution given in Equation (20) is difficult to solve. This equation can however be replaced by a first order equation using the fact that

$$g_{\mu\nu}\dot{x}^\mu\dot{x}^\nu = \begin{cases} -c^2, & \text{for timelike geodesics} \\ 0, & \text{for null geodesics}\,, \end{cases} \tag{21}$$

where a timelike orbit describes the orbit of a massive body, and a null orbit one of a massless body. Therefore, with $\theta = \pi/2$, the radial equation can be written in the more convenient first order form

$$-c^2 = -\left(1 - \frac{2GM}{c^2 r}\right)c^2\dot{t}^2 + r^2\dot{\phi}^2 + \left(1 - \frac{2GM}{c^2 r}\right)^{-1}\dot{r}^{\,2}. \tag{22}$$

This means that with $\theta = \pi/2$ the full set of equations describing the Schwarzschild geodesic orbits may be written as

$$\dot{t} = E\left(1 - \frac{2GM}{c^2 r}\right)^{-1}, \tag{23}$$

$$\dot{\phi} = \frac{L}{r^2}, \tag{24}$$

$$\dot{r}^2 = -\frac{L^2}{r^2}\left(1 - \frac{2GM}{c^2 r}\right) + c^2(E^2 - 1) + \frac{2GM}{r}. \tag{25}$$

Given a set of initial conditions and specifying the parameters of the orbit (the energy and angular momentum), the entire geodesic orbit can be calculated. The energy and angular momentum can, more conveniently, be specified in terms of the semi-latus rectum p and the eccentricity e of the orbit, which specify the orbit size and deviation from a circular orbit, respectively.

In Figure 2 we can see examples of the Schwarzschild geodesics along with a plot of the potential energy as a function of radius. In contrast to the Newtonian potential energy, there exists a new phenomenon in the Schwarzschild geodesics not found in the Newtonian case. The orbits of the geodesics precess for non-zero eccentricities. This means that the orbit revolves around the black hole, creating flower-petal patterns. Eventually, the orbit will fill the space between the maximum and minimum radii.

The precession for a Schwarzschild geodesic can be found analytically with Equation (25). By using the chain rule with ϕ and introducing the variable $u = 1/r$, the equation may be rewritten as

$$\frac{d^2u}{d\phi^2} = -u + \frac{GM}{L^2} + \frac{3GMu^2}{c^2}. \tag{26}$$

The presence of the last term $3GMu^2/c^2$ is a correction to the Newtonian equation, where the last term of Equation (26) is not present, and is due to the correction coming from General Relativity. An analytic solution for u exists for the Newtonian case and, assuming a weak gravitational field, the Newtonian solution can serve as a first order approximation to the u solution, namely

$$u = \frac{GM}{L^2}(1 + e\cos\phi) + \Delta u, \tag{27}$$

where e is the eccentricity of the orbit and Δu is a perturbation to the solution.

To first order in the small quantity Δu, we obtain

$$\frac{d^2\Delta u}{d\phi^2} + \Delta u = \frac{3(GM)^3}{c^2 L^4}(1 + e^2\cos^2\phi + 2e\cos\phi). \tag{28}$$

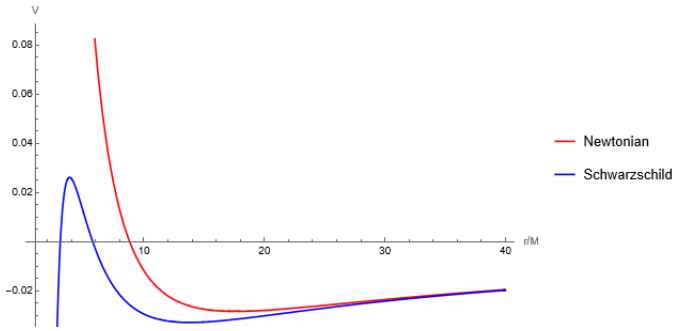

(a) The gravitational potential energy for a Newtonian system and a Schwarzschild system.

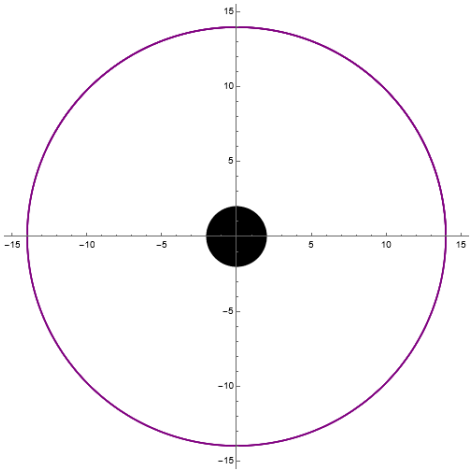

(b) A circular Schwarzschild orbit with zero eccentricity.

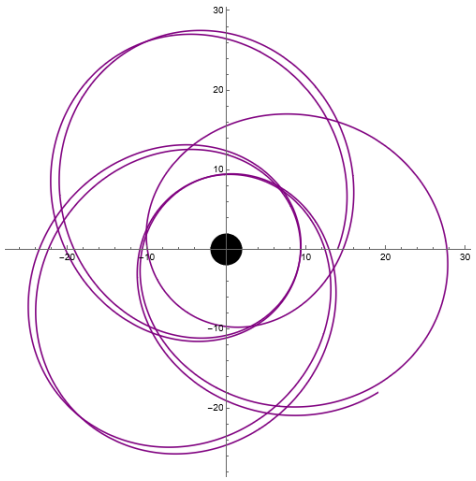

(c) The precession of the Schwarzschild orbit.

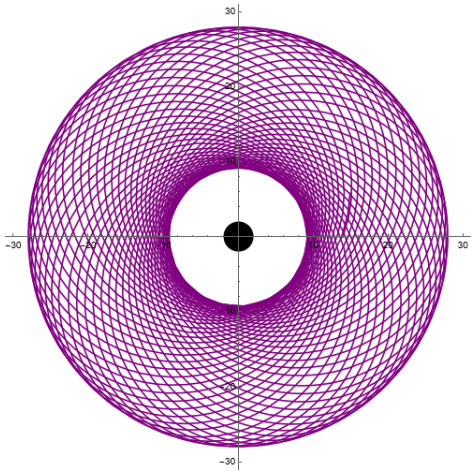

(d) The same precessing Schwarzschild orbit, integrated to long time.

Figure 2: The Schwarzschild solution produces interesting, precessing geodesics for non-zero eccentricities, differing from the Newtonian case. The orbits here have a semi-latus rectum $p = 14$. The circular orbit is of zero eccentricity while the latter two orbits are both of 0.5 eccentricity.

The solution to this equation is thus given as

$$\Delta u = \frac{3(GM)^3}{c^2 L^4}\left(1 + e^2\left(\frac{1}{2} - \frac{1}{6}\cos 2\phi\right) + e\phi\sin\phi\right) . \tag{29}$$

Since $3(GM)^3/c^2L^4$ is a small quantity, the first two terms of Equation (29) will oscillate around a small value. However the last term, which is proportional to the monotonically increasing ϕ variable, is cumulative and will grow over time. This term cannot be neglected in the full solution to u, which thus reads

$$u = \frac{GM}{L^2}(1 + e(\cos\phi + \beta\phi\sin\phi)) , \tag{30}$$

where $\beta = 3(GM)^3/(c^2L^4) \ll 1$.

Therefore, since $\cos(\phi(1-\beta)) \approx \cos\phi + \beta\phi\sin\phi$ for small β, we can write

$$u \approx \frac{GM}{L^2}(1 + e\cos(\phi(1-\beta)))\,, \tag{31}$$

showing that that orbit precesses. The difference in angle between the precessing orbit and an equivalent closing circular orbit over a full orbital period is approximately $2\pi\beta$, and we therefore obtain

$$\Delta\phi = \frac{6\pi GM}{a(1-e^2)c^2}\,, \tag{32}$$

where a is the semi major axis, given as

$$a = \frac{L^2}{GM(1-e^2)}\,. \tag{33}$$

The motion of the Schwarzschild geodesics is however confined to the plane $\theta = \pi/2$, since we are considering a non-rotating black hole. Most objects in the universe rotate however, and we must consider the case of a rotating black hole. The space-time generated by a rotating black hole is called the Kerr space-time and produces different orbits to those of the Schwarzschild case. These orbits are not confined to the equatorial plane and therefore we cannot neglect the dynamics of the geodesic equation for θ. The theory used to derive the Schwarzschild geodesics is however similar to the theory used to derive the Kerr geodesics, such as identifying constants of motion and writing the geodesic equations in terms of these constants. This not only aids in the understanding of Kerr geodesics, but the theory developed for the Schwarzschild space-time can serve as a useful approximation in later analysis of Kerr space-time.

2.2 Kerr Space Time

The case of the space-time metric generated by an uncharged, rotating black hole was discovered by Roy Kerr in 1963 [17]. The general form of the metric in Boyer-Lindquist coordinates and in geometrised units $G = c = 1$, is given as

$$ds^2 = -\left(1 - \frac{2Mr}{\Sigma}\right)dt^2 + \frac{\Sigma}{\Delta}dr^2 + \Sigma\,d\theta^2 + \left(r^2 + a^2 + \frac{2Ma^2r}{\Sigma}\sin^2\theta\right)\sin^2\theta\,d\phi^2 - \frac{4Mar}{\Sigma}\sin^2\theta\,dt\,d\phi\,, \tag{34}$$

where $\Sigma = r^2 + a^2\cos^2\theta$ and $\Delta = r^2 - 2Mr + a^2$. In this space-time, a is the *Kerr Parameter* of the black hole which describes the dimensionless spin of the black hole, defined as $a = J/M$ such that the spin of the black hole in units of the black hole mass, J, is divided by the black hole mass M.

The presence of the cross term $dt\,d\phi$ suggests a coupling to the azimuthal angle with time, predicting such phenomena as "frame dragging", which is when the coordinate system is dragged around with the rotating black hole [13]. The

geodesic equations are clearly more complicated for this space-time, however similarly to the Schwarzschild case, they can be solved by identifying constants of motion. Along with the usual constants of motion found in the Schwarzschild case, the energy E, the angular momentum L_z and the test particle mass μ (often set to unity), Brandon Carter identified the additional constant of motion Q, now known as *Carter's Constant*, which loosely describes the geodesic's non-axial angular momentum [18]. Carter showed that using these constants, the geodesic orbit is completely characterised by the following set of first order differential equations [19], given in geometrised units as

$$\left(\frac{dr}{d\lambda}\right)^2 = V_r(r) \equiv (E\bar{\omega}^2 - aL_z)^2 - \Delta(\mu^2 r^2 + (L_z - aE)^2 + Q)\,, \tag{35}$$

$$\left(\frac{d\theta}{d\lambda}\right)^2 = V_\theta(\theta) \equiv Q - L_z^2 \cot^2\theta - a^2(\mu^2 - E^2)\cos^2\theta\,, \tag{36}$$

$$\frac{dt}{d\lambda} = V_t(r,\theta) \equiv E\left(\frac{\bar{\omega}^4}{\Delta} - a^2\sin^2\theta\right) + aL_z\left(1 - \frac{\bar{\omega}^2}{\Delta}\right)\,, \tag{37}$$

$$\frac{d\phi}{d\lambda} = V_\phi(r,\theta) \equiv L_z \csc^2\theta + aE\left(\frac{\bar{\omega}^2}{\Delta} - 1\right) - \frac{a^2 L_z}{\Delta}\,, \tag{38}$$

where $\bar{\omega}^2 = r^2 + a^2$, and Δ and Σ are previously defined. The derivatives and the coordinates are with respect to an affine parameter different to the proper-time, namely *Mino Time*. Although first alluded to by Carter, Mino was the first to use this parameter to fully take advantage of the periodic nature of the Kerr orbits [20]. The definition of this Mino time is given as

$$\frac{d\tau}{d\lambda} = \Sigma = r^2 + a^2\cos^2\theta\,, \tag{39}$$

where τ is the proper time and Σ previously defined. If one were to instead derive the geodesic equations from Equation (34) with respect to proper time, they would see a coupling between $r(\tau)$ and $\theta(\tau)$, meaning that the differential equations for both of these coordinates would depend on the other. This greatly complicates the calculations of the geodesic orbits and it becomes computationally costly. Parameterising, however, with respect to Mino time, we can see a decoupling of the $r(\lambda)$ and $\theta(\lambda)$ equations in Equations (35) and (36), such that they are only functions of themselves for a given set of orbital constants. This means that solving the geodesic equations is much easier in Mino time than in proper time.

Instead of using the dimensionless constants of motion (E, L_z, Q), the geodesic orbits can be paramaterised by the more convenient set of parameters $(p, e, \theta_{\min})$, where p is the orbital semi-latus rectum, e is the eccentricity and $\theta_{\min}$ is the minimum polar angle reached by the three dimensional orbit. The relationship between these constants of motion was derived by Schmidt [21] and is outlined in the Appendix.

2.3 Geometrised Units

Using the International System of Units, SI units, is perfectly acceptable to calculate the geodesic equations and to analyse our results. However, typical astronomical values in SI units are extraordinarily large, or small, numbers. For example,

Newton's gravitational constant is approximately 6.6743×10^{-11} m^3 kg^{-1} s^{-2} while the speed of light is approximately 2.998×10^8 m s^{-1}. Working directly with these values would complicate analysis of the results and shroud intuition that could be gained. We can simplify our calculations and gain more physical intuition from calculations by using *geometrised units*, in which we choose units such that $G = c = 1$ [14].

Geometrised units are given in powers of length. In order to convert a quantity in SI units of [kg$^\alpha$ m$^\beta$ s$^\gamma$] to geometrised units of length [m$^{\alpha+\beta+\gamma}$], we multiply by the conversion factor

$$G^\alpha c^{\gamma-2\alpha}\,. \tag{40}$$

The conversions for common quantities is given in Table 3. Note that the inverse of the conversion factors can be applied to convert from geometrised units to SI units.

Conversion Factors			
Quantity	SI Unit	Geo. Unit	SI to Geo. Factor
mass	kg	m	$G\,c^{-2}$
length	m	m	1
time	m s^{-1}	m	c

Table 3: The conversion factors from SI units to geometrised units for common physical observables.

As an example, we can consider the mass of the Sun. In SI units this is quoted as approximately 1.989×10^{30} kg. Multiplying this by the factor $G\,c^{-2}$ we see that the Sun has a mass of approximately 1480m in geometrised units.

Furthermore, we can introduce a new set of units to parameterise the orbital quantities. Since the black hole mass in geometrised units has dimensions of length similar to the other geometrised quantities, we can parameterise lengths, times and other masses in units of the black hole mass. So, for example, given a value for the semi-latus rectum p in geometrised units, we can divide this value by the black hole mass in geometrised units to get the semi-latus rectum in units of the black hole mass, namely $\tilde{p} = p/M$, with p and M in geometrised units. This process also naturally extends to masses and times.

2.4 Numerical Calculation of Kerr Geodesics

The equations governing the Kerr geodesic orbits, Equations (35) to (38), may be solved numerically. The problem essentially consists of solving four ordinary differential equations with respect to Mino time λ. Certain physical considerations must however be kept in mind. The solutions to $t(\lambda)$ and $\phi(\lambda)$ are monotonically increasing functions and therefore given

an initial condition for each coordinate, the solutions can be found for all values of λ. However, the solutions for $r(\lambda)$ and $\theta(\lambda)$ are not monotonically increasing and have periodic turning points at their maximum and minimum values, leading to sign changes in the integrations of Equations (35) and (36). This means that initial conditions for r_0 and θ_0 are only valid until the turning points, upon which the integration of the first order differential equations must start again. The solution for these coordinates is therefore the result of integrating to the turning points, then resetting the initial condition, then repeating this process while stitching the solutions together. This method is impractical since we would need to change the equations of motion every time the orbit hits a turning point.

Another way to approach the numerical calculation of the geodesics is to recognise the oscillations of the $r(\lambda)$ and $\theta(\lambda)$ solutions between the turning points as the result of a second order differential equation, and to convert these equations to second order, while leaving the monotonically increasing $t(\lambda)$ and $\phi(\lambda)$ equations in first order. Therefore we require two initial conditions for the radial and polar angle trajectories. The initial condition for the coordinate velocity can however be obtained from the given Equations (35) and (36) themselves, given initial positions. Once the equations and initial conditions are given, the system of differential equations may be solved numerically. The software MATHEMATICA was used in this project to numerically solve the Kerr geodesics.

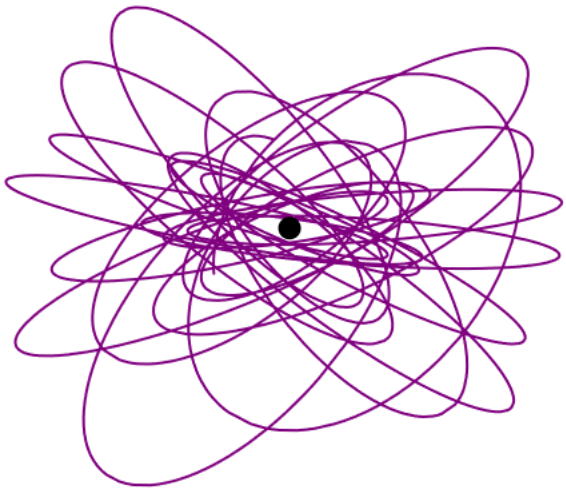

(a) The three-dimensional orbit around the black hole.

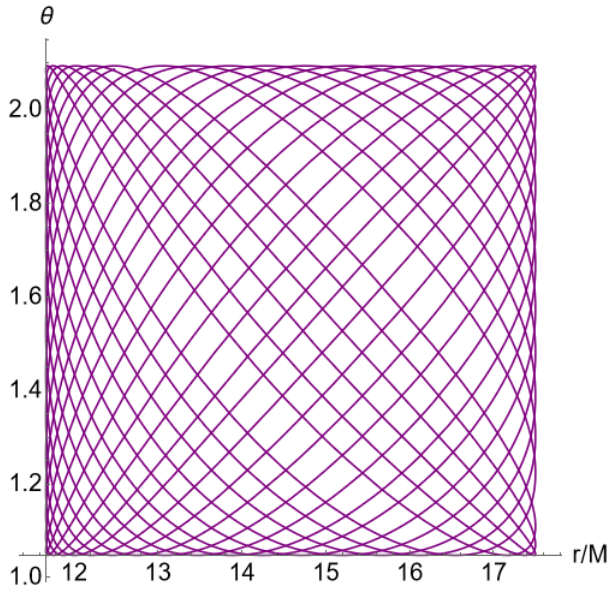

(b) The orbit plotted in r-θ phase space. The confining box represents a toroidal region around the black hole.

Figure 3: A generic Kerr geodesic trajectory, with Kerr orbital parameters $a = 0.7$, $p = 14$, $e = 0.5$ and $\theta_{\min} = \pi/4$.

The results of numerically calculating the Kerr geodesic equations can be found for a generic case in Figure 3. We see that the spin of the black hole means that the geodesic orbit is not confined to the equatorial plane. Furthermore, the geodesic orbit eventually fills up the space in a toroidal region around the black hole, between the minimum and maximum radii,

given by

$$r_{\min} = \frac{p}{1+e}\,, \qquad r_{\max} = \frac{p}{1-e}\,, \tag{41}$$

and the minimum and maximum polar angles. The maximum polar angle is $\theta_{\max} = \pi - \theta_{\min}$ by symmetry.

3 Modelling the OJ 287 System

"It can scarcely be denied that the supreme goal of all theory is to make the irreducible basic elements as simple and as few as possible without having to surrender the adequate representation of a single datum of experience." - Albert Einstein in a 1933 lecture. [22]

The basic model of the OJ 287 system is as a supermassive binary black hole in which an accretion disc surrounds the primary black hole while a secondary black hole, of much less mass, orbits around the primary. We may introduce a number of approximations into our model in order to simplify the analysis.

Firstly, since the vast majority of astrophysical bodies in the universe rotate, we assume the primary black hole is rotating and therefore the space-time surrounding the black hole is the Kerr space-time. We reject the possibility of a Kerr-Newman black hole, in which the black hole has a non-zero charge, since the primary black hole is surrounded by an accretion disk on the equatorial plane, and infalling, charged matter would cancel the charge of the black hole.

Since the ratio of the black hole masses is assumed much less than unity, the geodesic equations are used as a zeroth order approximation to the true trajectory of the secondary black hole. We therefore treat the secondary black hole as a test particle which follows a geodesic in the Kerr space-time around the primary black hole, in the assumption that it adequately approximates the true trajectory. The previously discussed theory regarding Kerr space-time and the corresponding geodesics can therefore be applied to the modelling of this system.

As the two black holes of finite mass orbit each other they emit gravitational waves, which are ripples through space-time [19]. The gravitational waves radiate energy away from the system and therefore the orbit of the secondary black hole around the primary decays over time. The effect of the energy of the orbit decreasing is to reduce the orbital parameters p, e, θ_{min} such that the size of the orbit becomes smaller, the orbital shape becomes more circular, and the orbit becomes more confined to a plane. In the true system, the orbit should decay *adiabatically*, meaning that the orbit evolves slowly and "constant" parameters of the system, such as the energy, should decay slowly relative to the typical orbital period [19]. Previous investigations of the OJ 287 system have applied this theory and obtained a merging of the two black hole within $10,000$ years [4]. In our investigation however we neglect the energy loss of the system due to radiation reaction emission of gravitational waves and assume the orbital constants E, L_z, Q to remain constant. This approach is an obvious

approximation, however justified since we analyse the system over a span of approximately 100 years, as given in Table 1.

The astrophysical considerations of the accretion disk are complex. Strictly speaking, the accretion disk thickness, density and other factors are a function of the radial coordinate from the primary black hole [1]. When the orbiting secondary black hole interacts with the accretion disk, the time of the emitted burst of light intensity differs from that of the time of impact with the accretion disk. The time of outburst is firstly advanced by the gravitational attraction of the secondary black hole. The tidal forces and gravitational force from the secondary work to attract the accretion disk material from the equatorial plane and interact with the secondary black hole before the secondary reaches the original position of the accretion disk. There exists also a time delay, which delays the time of outburst from the time of impact. When the secondary black hole interacts with the accretion disk a bubble of expanding plasma is created, which is assumed to be the cause of the burst in light intensity. However, the plasma bubble is originally optically thick, letting no light be released from its hot interior until the bubble expands and cools enough to become optically thin, allowing the internal radiation to escape. This functions as the aforementioned time delay. These time advances and delays are related to the outburst time as

$$t_{\text{outburst}} = t_{\text{impact}} - t_{\text{advance}} + t_{\text{delay}} \,. \tag{42}$$

In order to simplify the analysis, we assume that the accretion disk is uniform, infinitely thin and extends along the entire equatorial plane. It is assumed that the time of impact is equal to the time of outburst, meaning that we neglect the time advances and delays caused by the astrophysical considerations of the accretion disk. The time of impact is assumed to be when the secondary black hole crosses the equatorial plane of the primary, at $\theta = \pi/2$. We also assume that the interactions with the accretion disk do not alter the trajectory of the orbiting secondary black hole.

Considering these assumptions and the theory of Section 2.2, the entire geodesic orbit of the secondary black hole can be characterised by the parameters $a, p, e, \theta_{\text{min}}, M, r_i$ and θ_i, where a is the dimensionless Kerr-parameter measuring the spin of the black hole, p is the semi-latus rectum which characterises the size of the orbit, e is the orbital eccentricity, θ_{min} is the minimum polar angle reached by the orbit, M is the mass of the primary black hole, r_0 is the initial value of the radial coordinate and θ_0 is the initial polar angle. The initial azimuthal angle ϕ_0 and the initial coordinate time t_0 are taken as zero.

In our analysis of the OJ 287 system, we wish to calculate the orbits, predict the outburst times and compare these with the recorded outbursts from Table 1. We assume, as previously discussed, that the outburst times correspond to the times of intersection between the orbit and the $\theta = \pi/2$ equatorial plane, which is where the accretion disk is assumed to lie. The integration of the orbit is modelled to begin at the first recorded intersection time and therefore the initial polar angle $\theta_0 = \theta(0)$ must equal $\pi/2$, reducing the number of orbital parameters we need to consider.

The initial radial coordinate $r_0 = r(0)$ may also be set to an arbitrary value, within the constraints of the orbital con-

stants, meaning $r_{\min} \leq r \leq r_{\max}$ and $\theta_{\min} \leq \theta \leq \theta_{\max}$. Once the parameters a, p, e, M and $\theta_{\min}$ are set, and once we take $\theta_0 = \pi/2$, the initial radius only corresponds to a simple phase of the orbital precession. With the orbital constants already set, the orbit precesses around the primary black hole, with the radii at the intersection points of $\theta = \pi/2$ being swept around the primary black hole. Since the Kerr black hole is rotationally invariant around the ϕ angle, we assume all phases to be equivalent and are therefore free to choose any r_0 within the constraints of the orbital constants. For convenience, the initial radial coordinate for every orbital evaluation is taken to be $r_0 = 1.5p$ where p is the semi-latus rectum.

Given these considerations, we therefore wish to estimate the set of parameters $a, p, e, \theta_{\min}, M$ which predict outburst times which most closely match those of observation.

4 Parameter Estimation

"Science makes no pretension to eternal truth or absolute truth."

- Eric Temple Bell.

4.1 Obtaining the Intersection Points

Comparing predictions to observations means that the outburst times must be calculated for a given set of orbital parameters. This means that, given a set of orbital parameters $a, p, e, \theta_{\min}$, the intersections of the orbit with the $\theta(\lambda) = \pi/2$ plane must be found. Since the solutions to the polar angle and the coordinate time, from Equations (36) and (37), are calculated numerically, the intersections must also be found numerically which essentially corresponds to a numerical root finding algorithm. Table 4 gives an overview of the algorithmic steps taken to find the intersections.

Each value for θ in the solution to the polar angle is checked for the criterion that $\theta(\lambda) = \pi/2$, within the precision of the integration step over Mino time λ. The first and last values from the list of polar angles should be checked. If they are equal to $\pi/2$ they correspond to intersection points and should be saved. Excluding the endpoints, every other value for θ must be checked, which is performed by comparing neighbouring θ values, which is why the endpoints must be checked first. For every ith index value of the polar angle, if $\theta[i] < \pi/2$ and $\theta[i+1] > \pi/2$, this corresponds to an intersection at the index i where the orbit is moving from above the accretion disk to below it. Similarly, if $\theta[i] > \pi/2$ and $\theta[i+1] < \pi/2$ this corresponds to an intersection at index i where the orbit moves from below the accretion disk to above it. This completes the possible cases for intersections and returns the list of the indices for which intersections occur. Figure 4 shows a graph of a polar angle solution as a function of Mino time, along with the numerically found intersection points. The intersection on lines of positive slope correspond to the orbit moving from above to below the accretion disk, while those of negative slope correspond to moving from below to above the accretion disk. As expected, all intersection points are found and lie along the $\theta(\lambda) = \pi/2$ line, to within the precision of integration of the Kerr geodesics.

Algorithm to Numerically Extract the Intersection Times	
1)	Extract the list of all θ values from the calculated geodesic.
2)	Check the first entry of the θ values. If it equals $\pi/2$ return 1. If not then return nothing.
3)	Check θ values between the second and second last, inclusive. For index i, if $\theta[i] < \pi/2$ and $\theta[i+1] > \pi/2$ return i. or if $\theta[i] > \pi/2$ and $\theta[i+1] < \pi/2$ return i.
4)	Check the last entry of the θ values. If it equals $\pi/2$ return the length of the list of θ values. If not then return nothing.
5)	Join the lists from steps 2 - 4 together to create a list of indices for the intersections.
6)	For each index in the list of indices extract the coordinate time t at that index from our geodesic results and merge the values together to create the list of intersection times.

Table 4: The algorithmic steps taken to extract the intersection times, given an already numerically calculated geodesic orbit.

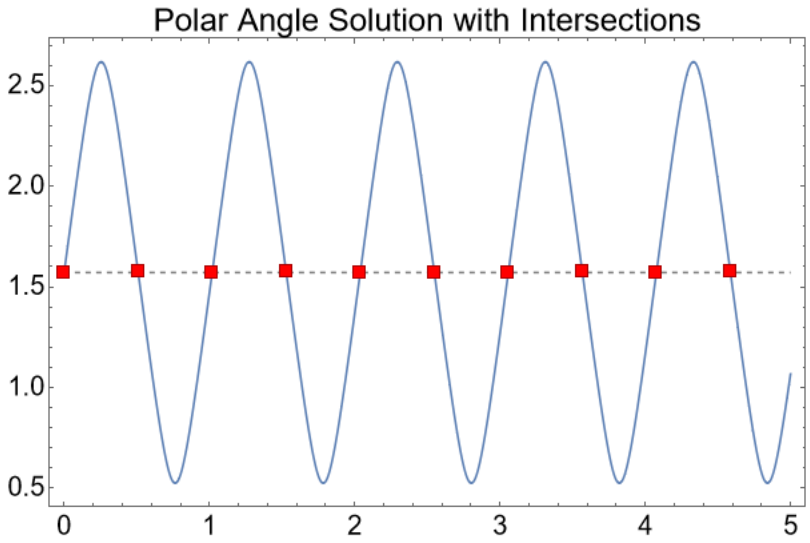

Figure 4: The polar angle coordinate as a function of Mino time for the optimal solution to the OJ 287 system. The intersections are marked with red dots. Note that they all lie on the value $\theta = \pi/2$, as expected, corresponding to the plane of the accretion disk.

This particular algorithmic procedure is both useful and necessary for two reasons. Firstly, due to the finitely sized discrete integration over Mino time it is not guaranteed that the polar angle will equal $\pi/2$ exactly, rather two consecutive points could lie below and above the $\pi/2$ line, or vice versa. The discussed intersection algorithm ensures that an approximate intersection point will be found even if the polar angle does not equal $\pi/2$ exactly. Secondly, the outlined algorithm ensures that there is no double counting at the intersection points, in which consecutive values would be chosen at each

intersection point. This would occur if our algorithm naively checked the condition that for a given ith polar angle value, the preceding value is less than $\pi/2$ and the succeeding greater than $\pi/2$, or the preceding greater than $\pi/2$ and the succeeding less than $\pi/2$. This criteria would be satisfied for two consecutive points on either side of the $\pi/2$ line and the indices of two consecutive points would be returned. The algorithm outlined in Table 4 avoids this problem.

The indices of this list of intersection points can be matched to the list of the coordinate times t, since these times are evaluated at the same points as the polar angle θ (and the other coordinates r and ϕ). The coordinate times at each of the intersection indices can be saved to a list, giving back the intersection times. Since Equations (35) to (38) are used, the times are in geometrised units of the primary black hole mass. This can be converted into SI units using the conversion factors of Section 2.3.

4.2 Fitting for the Parameters

A comparison between predicted and observed outburst times can be made given the set of orbital parameters $a, p, e, \theta_{\text{min}}$ and M. The intersection times of the Kerr geodesic solution can be calculated in geometrised units of the black hole mass using the theory of Section 2.3, the observed outburst times can be converted to geometrised units of that given black hole mass and then a fit of the root mean squared deviation between the two times can be made, namely

$$\text{RMS} = \sqrt{\frac{1}{N}\sum_{i=2}^{N}\left(\frac{P_i - O_i}{O_i}\right)^2}, \tag{43}$$

where P_i is the ith predicted outburst time, O_i is the ith observed outburst time and N is the number of observed outbursts.

It is noted from Table 1 that there are ten observed outbursts and so $N = 10$. In order to make sure that the length of the lists of predicted and observed outbursts are the same, such that a comparison can be made, the Kerr geodesic is integrated to large Mino times and then the first ten values of the list are extracted in order to be compared with the observed times. This avoids any complications with list lengths not matching.

Note that the difference of the predicted and observed outburst times in Equation (43) are normalised by the value of the observed outburst time, O_i, giving a fractional difference. This is introduced to facilitate comparison between the outburst times in geoemtrised units of the black hole mass for different masses of the primary black hole. The magnitude of the observed outburst times in geometrised units of the black hole mass becomes smaller as the black hole mass increases, since the period of outburst times in SI units must remain constant at about 12 years. Therefore the RMS deviation of the predicted outbursts from the observed outbursts would inevitably be smaller due to the lower absolute values of the geometrised times in black hole mass units. This would lead to an ever decreasing least squares fit as the black hole mass increases, which is incorrect. Normalising the difference by dividing by the observed time gives a fractional difference,

which can then be compared with results of other black hole masses, with the fit made in geometrised units of the black hole mass.

4.3 Scanning over Parameter Space

In order to fit for the Kerr geodesic parameters which minimise the difference between the predicted and observed outburst times, a scan over the parameter space must be made. There are different ways to scan through parameter space, however the approach taken in this investigation is a multidimensional grid scan. A range of scanning values for each of the parameters $a, p, e, \theta_{\min}$ and M are specified, each with a minimum and maximum scanning value and a scanning step size. The intersection times for each combination of parameters is found, and the normalised root mean squared deviation with the observed outburst times assigns a "fit value" to that set of parameters. The set of all combinations can be thought of as a grid in n dimensional space, where n is the number of parameters being scanned, while scanning over the possible combinations can be interpreted as moving through the grid of combinations. In this case $n = 5$.

This approach, although straightforward, is computationally expensive. Rather than scanning over the entire parameter space with a large range of values and a short scanning step size for each parameter, an initial coarse scan can be made. In the approach taken in this investigation, a coarse scan over the mass of the primary black hole is made, the optimum Kerr geodesic parameters are found for that mass and the resulting minimum least squares value is attached to that mass.

As an initial guess for the mass of the system, we may use a combination of Kepler's Third Law, and Equation (32) which quantifies the precession of an orbit.

$$\text{Kepler's Third Law} \Rightarrow T_{1/2}^2 = \frac{\pi^2 a^3}{GM}\,, \tag{44}$$

$$\text{Orbital Precession} \Rightarrow \Delta\phi = \frac{6\pi GM}{c^2 a(1-e^2)}\,, \tag{45}$$

where in this case $T_{1/2}$ is equal to half of the orbital period. These equations can be used to eliminate the semi-major axis a and provide an estimate for the mass in terms of half the orbital period and the orbital precession

$$M = \left(\left(\frac{G\,T_{1/2}^2}{\pi^2}\right)^{1/3}\left(\frac{c^2(1-e^2)\Delta\phi}{6\pi G}\right)\right)^{3/2}\,. \tag{46}$$

In this sense, a range of the masses which give the lowest values for the least squares fit can be found. This provides the basis for a *finer scan* over the masses, performed within that range of "minimums". Due to the computationally cost of scanning over parameter space, the black hole mass with the minimum least squares fit value from this finer scan is taken to be the "true" value of the primary black hole mass. Using this value for the primary black hole mass, a fine scan over the parameters a, p, e and $\theta_{\min}$ may be performed. The resulting set of parameters with the least squares fit value for this

fine scan are taken as the true parameters of the system describing OJ 287.

5 Results

From Figure 1 it is observed that there are two main periods in the orbit, which occur over a 12 year range and a 60 year range. Interpreting these quantities as the orbital period and the precession period, we see

$$\frac{60}{12} = \frac{180 \text{ degrees}}{\Delta\phi} \quad \Rightarrow \quad \Delta\phi = \frac{12 \times 180}{60} = 36 \text{ degrees} = 0.628319 \text{ rad}\,. \tag{47}$$

with $\Delta\phi$ the estimated precession phase advance.

Meanwhile, from previous investigation it is noted that the eccentricity should be approximately 0.7 [7].

Using these estimate values, Equation (46) serves as a rough estimate for the total system mass in order to begin the parameter space scan. The initial estimate of the OJ 287 system mass is placed at 54 billion $\mathrm{M}_\odot$, with units of solar masses. However, this value is an overestimate. Equation (32) only accounts for the first order corrections from General Relativity and fails to include the higher order correction which would increase the value for the precession rate and thus also the mass. Secondly, in reality the true system consists of both a primary black hole and a secondary black hole, while the previously described equations use the total system mass M.

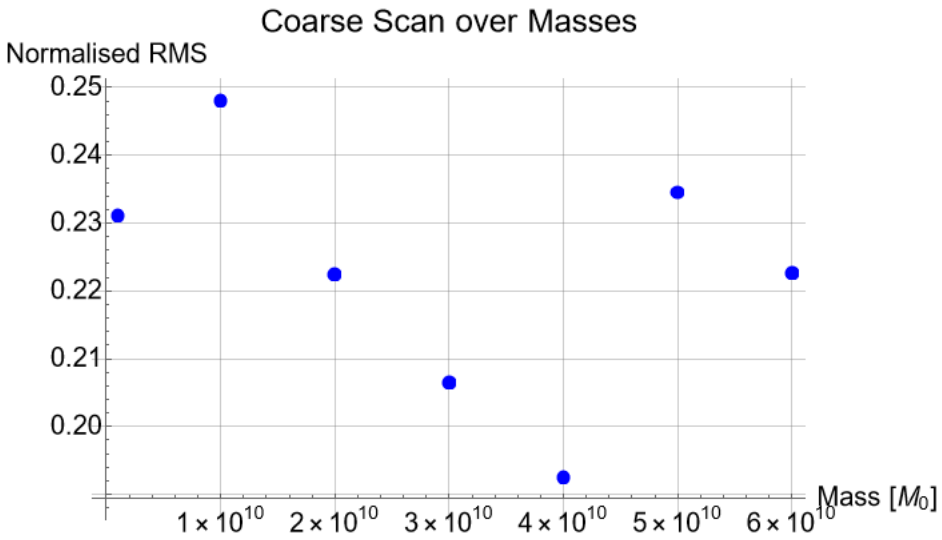

Figure 5: The normalised root mean square analysis of the optimum $a, p, e, \theta_{\min}$ values, coarsely scanned over a broad range of black hole masses.

Therefore the coarse parameter scan over the masses is performed using this estimate, over the mass range from $1 \times 10^9\,\mathrm{M}_\odot$ to $6 \times 10^{10}\,\mathrm{M}_\odot$ in steps of $1 \times 10^{10}\,\mathrm{M}_\odot$. The normalised root mean squared deviations for each set of parameters $a, p, e, \theta_{\min}$

are calculated. The value for the optimum set of parameters for each mass is plotted in Figure 5, showing a minimum around the region from approximately $2 \times 10^{10}\,\mathrm{M}_\odot$ to $4.5 \times 10^{10}\,\mathrm{M}_\odot$. Using the range from $2 \times 10^{10}\,\mathrm{M}_\odot$ to $4.5 \times 10^{10}\,\mathrm{M}_\odot$ a finer scan, in steps of $2 \times 10^{9}\,\mathrm{M}_\odot$, over the masses is performed, following the same procedure as previously described for the coarse scan. The range that the parameters $a, p, e, \theta_{\mathrm{min}}$ are scanned over are also adjusted. The results for this finer scan are shown in Figure 6. The minimum normalised root mean squared value occurs at a mass of $3 \times 10^{10}\,\mathrm{M}_\odot$, which is henceforth taken as the system mass.

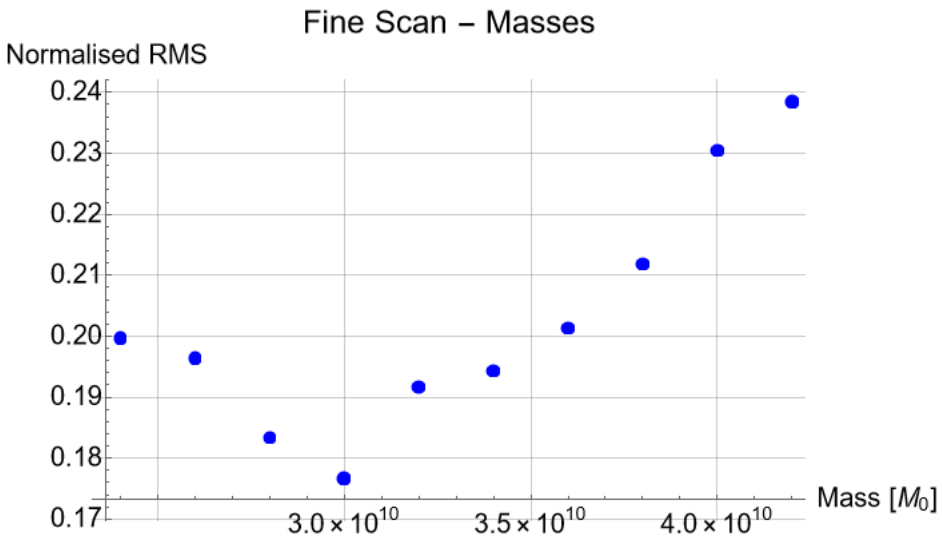

Figure 6: The normalised root mean square analysis of the optimum $a, p, e, \theta_{\mathrm{min}}$ values, finely scanned over a narrow range of black hole masses around the minimum of the coarse scan.

Given the mass of $3 \times 10^{10}\,\mathrm{M}_\odot$, a fine scan over the system parameters is performed. Table 5 gives an overview of the ranges and step sizes used in the scan. The parameters a and p are given in geometrised units of the black hole mass.

	a	p	e	θ_{min}
Min	0.1	20	0.4	$\pi/6$
Max	0.8	110	0.8	$\pi/3$
Step	0.1	1	0.1	$\pi/18$

Table 5: The ranges used for the fine scan over parameter space, given a primary mass of 30 billion solar masses.

There is a rationale for choosing the particular ranges and step sizes in Table 5 for the fine parameters scan. Not much information is provided, nor obtained from observation, in regards to the Kerr parameter a of the OJ 287 system. However since the observed outbursts occur with some periodicity, the spin parameter is not assumed to tend toward the maximum value of unity and the range over a is taken from 0.1 to 0.8 in steps of 0.1. The semi-latus rectum of the orbit p influences the period the most and therefore a wide ranging scan of this variable is taken. This approximate relationship is justified

by Kepler's Third Law, Equation (44), which relates the square of the orbital period to the cube of the semi-major axis, $T^2 \propto a^3$. Since the semi-latus rectum is closely related to the semi-major axis, and is just another measure of the orbital size, it can be justified that it has the greatest effect on the orbit. From literature [7] the eccentricity is thought to be between 0.6 and 0.7, therefore a shorter scanning range is used taking this empirical fact into account. The minimum polar angle $\theta_{\min}$ is scanned within a range of reasonable values. By "reasonable", it is assumed that since the intersections with the accretion disk produce very distinct light outbursts, as seen in Figure 1, the minimum polar angle must lie sufficiently far away from the accretion disk such that the secondary black hole is not constantly interacting with it. The upper bound for $\theta_{\min}$ is thus arbitrarily chosen as $\pi/3$. Meanwhile, unphysical orbits begin to emerge for Kerr geodesics with small values of the minimum polar angle, and a large enough minimum bound is required to be valid over all parameter combinations. The value $\pi/6$ is arbitrarily chosen as the lower bound for the minimum polar angle of the orbit.

Running the scan gives a result for the optimum parameter values for the Kerr geodesic. These are found to be $M = 3 \times 10^{10}\,\mathrm{M}_\odot$, $a = 0.1$, $p = 34$, $e = 0.8$ and $\theta_{\min} = \pi/6$, where a and p are in units of the black hole mass.

The relationships between the scan of the orbital parameters a, p, e and $\theta_{\min}$ parameters for the least squares fit between the predicted and observed intersection times in shown in Figure 7. Plotted in each subplot is the normalised root mean squared deviation between the predicted and observed times. The distribution over two parameters at a time is shown, while the other parameters are kept constant at the optimum values. Lighter colour values correspond to higher root mean squared deviation value meaning a worse fit with observation. The contours can be interpreted as a graphical representation of numerically found partial derivatives of the parameters. Therefore we can qualitatively see the effect of each parameter on the least squares fit, and the strength of its influence on the fit. The contours for $\theta_{\min}$ and for a against both p and e are essentially vertical lines, with the contour variation over the p and e parameters. This means that the semi-latus rectum and the eccentricity affect the orbit and the intersection times significantly more than the spin of the black hole and the minimum polar angle. These graphs also show that the fit is optimised for low values of the semi-latus rectum, within the range scanned, and high values of the eccentricity, within the range scanned. Most notably for the semi-latus rectum p, the large variation in the least squares values as the parameter is varied demonstrates a strong correlation between the orbit size and the intersection times, justifying the aforementioned claim that the semi-latus rectum has the greatest effect on the orbit and the resulting large scanning range for p. The optimum value for the semi-latus rectum $p = 34$ in geometrised units of the black hole mass translates into an SI unit value of 1.51×10^{15} m, which is approximately $10,070$ Au. This corresponds to $r_{\min} = 5,595$ Au and $r_{\max} = 50,350$ Au.

The bottom right graph of Figure 7 shows the variation of the fit while varying over the spin of the black hole and the minimum polar angle of the orbit. The contour lines suggest a slight preference of strength for the spin of the black hole in determining the orbit. The legend of the graph shows a least squares fit range between 0.178 and 0.192. Firstly, these

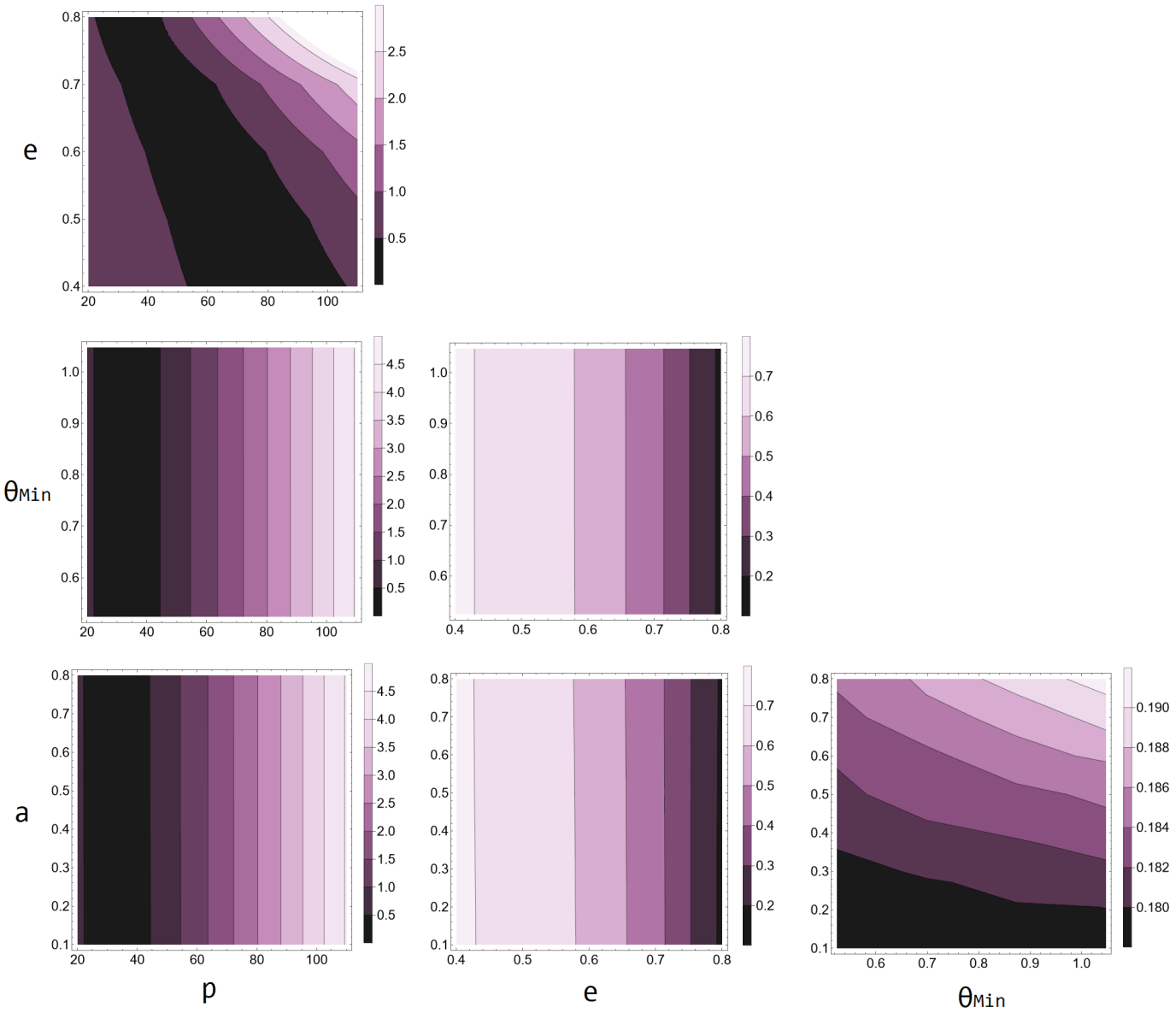

Figure 7: Contour plots of the normalised least squares fit for a primary black hole of 30 billion M_0, showing the relationships between the parameters of the system. The horizontal axes are sorted by column while the vertical axes by row. Darker colours indicate a lower root mean squared deviations and thus a better fit with observation. The Kerr parameter a and the semi-latus rectum p are in units of the black hole mass, the polar angle θ in radians and eccentricity e, a dimensionless quantity.

values are small compared to the least squares values for the other graphs and secondly the range is very narrow. This suggests that the variation in the least squares fit is being dictated by the other parameters p and e which are being held constant at the optimum values for this graph. The variation over these parameters p and e are found in the upper left graph of Figure 7. Strong variations for the least squares fit result from varying these two parameters. A greater value for the semi-latus rectum necessitates a lower value for the eccentricity in order to obtain a minimum of the least squares fit, while a lower semi-latus rectum necessitates a higher eccentricity, suggesting an inverse relationship between the two for

the optimum solution. This is explained with Equations (44), Kepler's third Law, and (45), the orbital precession rate. We can rearrange these equations to obtain

$$T^2 = \frac{6\pi^3 a^2}{\Delta\phi c^2(1-e^2)}\,, \tag{48}$$

where T is half the orbital period, a is the semi-major axis (which is related to the semi-latus rectum) and e is the eccentricity, giving us the relationship $T^2 \propto a^2/(1-e^2)$. In order to keep a constant T to match observations, if we increase the semi-latus rectum, the denominator of (48) must increase, meaning that the eccentricity must decrease, and vice versa.

We can also see that a degeneracy for the optimum solution values in the range scanned does not happen due to the relationships in Figure 7. The minimums of the least squares fit suggest the low eccentricity, small orbital size and low minimum polar angle, as found in the optimum solution.

The contour plots of Figure 7 do suggest, however, that the range of values scanned were not centred around the optimum values. The minimums of the least squares fit occur at the bottom of the scanned semi-latus rectum values, the top of the scanned eccentricity values and the bottom of the minimum polar angles values. The optimally found solutions $a = 0.1$, $p = 34$, $e = 0.8$ and $\theta_{\min} = \pi/6$ lie on the edge of the scanned ranges and therefore suggest a further scan be performed at those ends of the scanning ranges.

Given our optimum parameters, we can investigate the intersection times and compare the outbursts with observations. Table 6 presents the observed outburst times, the calculated outburst times from the optimum solution and the difference between the two, all in Julian years. Although not a perfect fit, the predicted times capture the rough behaviour of the OJ 287 system. The maximum deviation of a calculated outburst from its corresponding observed outburst is approximately 16.9 years which, assuming an outburst period of 12 years, is about 1.4 times the orbital period. The average magnitude of the deviation from the observed outbursts is approximately 8.64 years, which, again assuming a true outburst period of 12 years, is approximately 72 percent of an outburst period.

Outburst Times in Julian Years										
Observed	1912.980	1947.283	1957.095	1972.935	1982.964	1984.125	1995.841	2005.745	2007.6915	2015.875
Calculated	1912.98	1938.87	1940.18	1966.13	1967.81	1991.6	1995.57	2009.79	2023.36	2027.56
Difference	0	-8.41086	-16.9195	-6.80326	-15.1529	7.4782	-0.270364	4.04509	15.6685	11.6844

Table 6: The observed and calculated outburst times along with their difference, all in Julian years.

Figure 8 plots the coordinate time t against Mino time λ, with the outburst points marked with red dots. The coordinate time is a monotonically increasing function of Mino time, however exhibits alternating steep and shallow slopes. The outbursts occur, for the most part, on the shallow slopes of the $t(\lambda)$ solution. This means that the change in coordinate time, the time we see from a distance i.e. the Earth, is short between outbursts which corresponds to the secondary black

hole plunging towards and around the primary black hole, emitting a double light intensity burst. This agrees well with the model providing good justification for the model of the supermassive binary black hole.

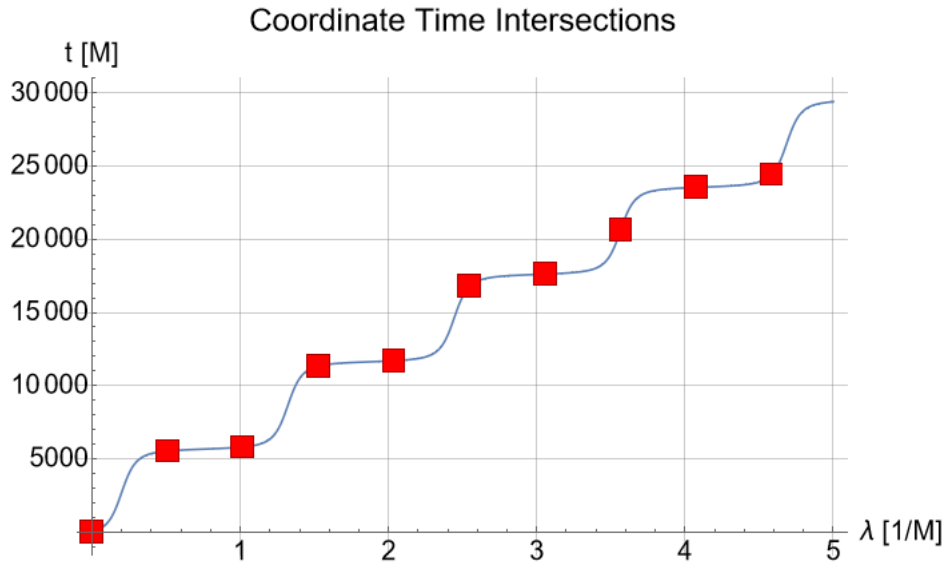

Figure 8: The coordinate time in units of the geometrised black hole mass of the optimum solution as a function of Mino time. The outbursts are marked with red dots.

The optimum solution to the Kerr geodesic orbit in three dimensions is plotted in Figure 9. Due to the low Kerr parameter of the primary black hole, the orbit is approximately confined to a disk-like plane and due to the low value of the minimum polar angle of $\pi/6$, this approximate disk of the orbit extends sharply out of the accretion disk. Several viewpoints are shown for completeness.

A top-down view is shown in Figure 10 with the outbursts again plotted with red markers. Note that the azimuthal angle ϕ has been shifted in this plot so as not to confuse the data with the arbitrarily chosen axes. This can be done due to the rotational symmetry of a Kerr black hole around the azimuthal angle. Due to the large inclination angle of the orbit, given from the small minimum polar angle, the orbit appears to extend almost vertically from the plane of the accretion disk. Therefore the outburst points appear to line up as the trajectory precesses around the black hole.

Finally, the trajectory is shown in phase space in Figure 11. The solution is confined to the toroidal region around the black hole between the minimum and maximum radii and the minimum and maximum polar angles, as expected for a Kerr black hole. The outburst points all lie along the $\theta = \pi/2$ line, corresponding to interactions with the accretion disk.

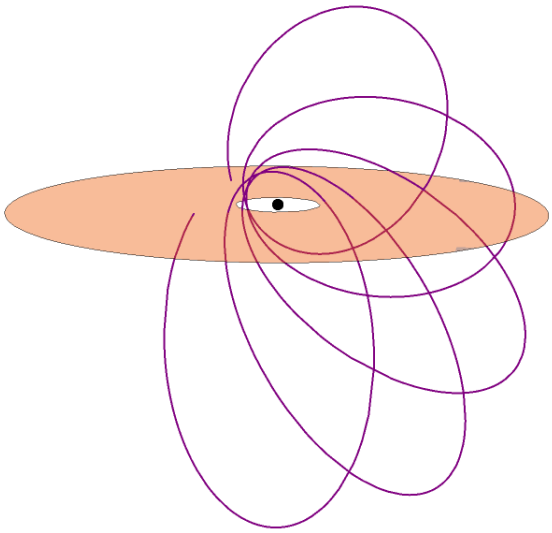

(a) Off-axis view of the orbit.

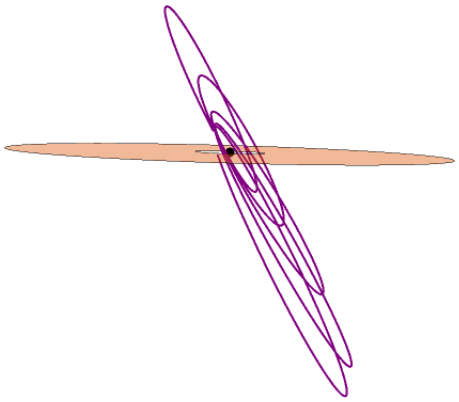

(b) View of the orbit within the approximate plane of the accretion disk.

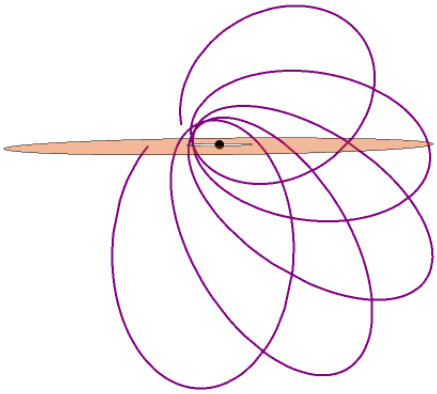

(c) An off-axis view of the orbit showing the orbital precession.

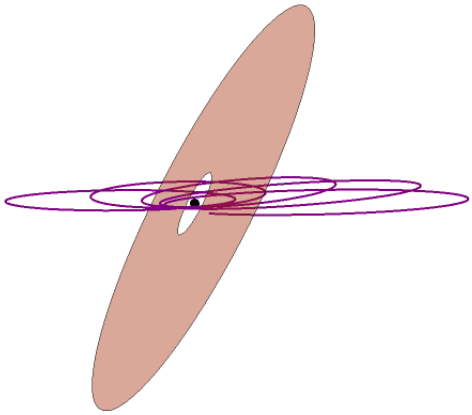

(d) View of the orbit within the approximate plane of the orbit.

Figure 9: The three dimensional plot of the orbit for the optimum values $a = 0.1$, $p = 34$, $e = 0.8$, $\theta_{min} = \pi/6$, viewed from four different angles. The accretion disk width and black hole size are not to scale.

6 Discussion

As previously alluded to, there are a number of improvements which can be made both to the model and the parameter scanning in order to improve the fit of the outbursts, found in Table 6.

Firstly, the orbital model for the secondary black hole used in this investigation are the Kerr geodesics. These assume that the secondary body is a test mass particle of negligible mass, which is unrealistic. The Kerr geodesics serve as a zeroth order approximation to the true path of the secondary black hole, however higher order corrections must take the

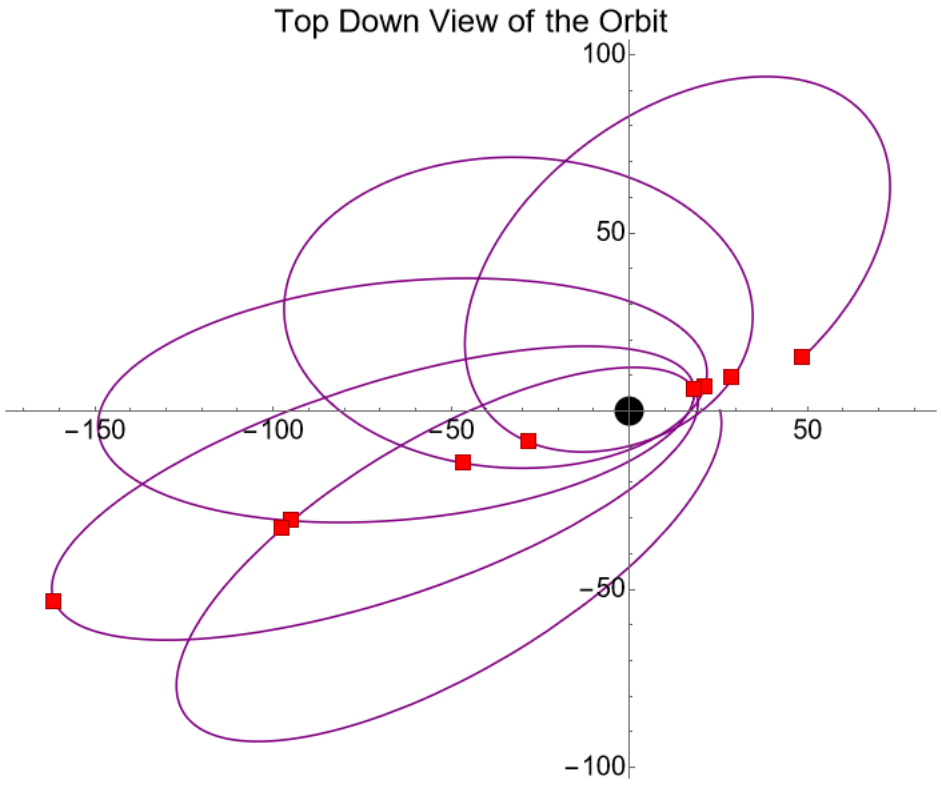

Figure 10: The top-down view of the solution orbit. Intersection points with the accretion disk corresponding to outbursts marked with red dots. Note that the azimuthal angle has been shifted in this plot so as not to confuse the data with the arbitrarily chosen axes. Distances are in geometrised units of the black hole mass.

mass ratio between the secondary and primary black holes into account. This mass ratio is assumed small, hence why the Kerr geodesics serve as a useful approximation. The equations of motion expanded in the ratio of the masses could then be used to model the true trajectory of the secondary black hole.

The outburst times given in Table 1 and therefore used in this investigation are only given up to the year 2015. Since then, there has been another recoded outburst [2]. Including this extra outburst could serve in either of two ways in order to improve the fit of the model. The outburst could be included as an extra data point in the least squares fit, bringing the total from ten to eleven recorded outbursts, which would provide a better statistical fit. Or the extra outburst could serve as a model validator, for which the predictions from a least squares fit using the first ten outbursts could be tested to predict the most recent outburst. In essence, these are two separate ways of going about the same thing, which is to improve the fit of the model using more data points.

The details of the behaviour of the interaction between the secondary black hole and the accretion disk are not included in this work. Incorporating the time advances and delays of Equation (42) by understanding the astrophysics of the accretion disk would give a more accurate relationship between the time of intersection and the time of outburst. Including these values with a description of the thickness of the accretion would also allow the light intensities to be predicted, along with

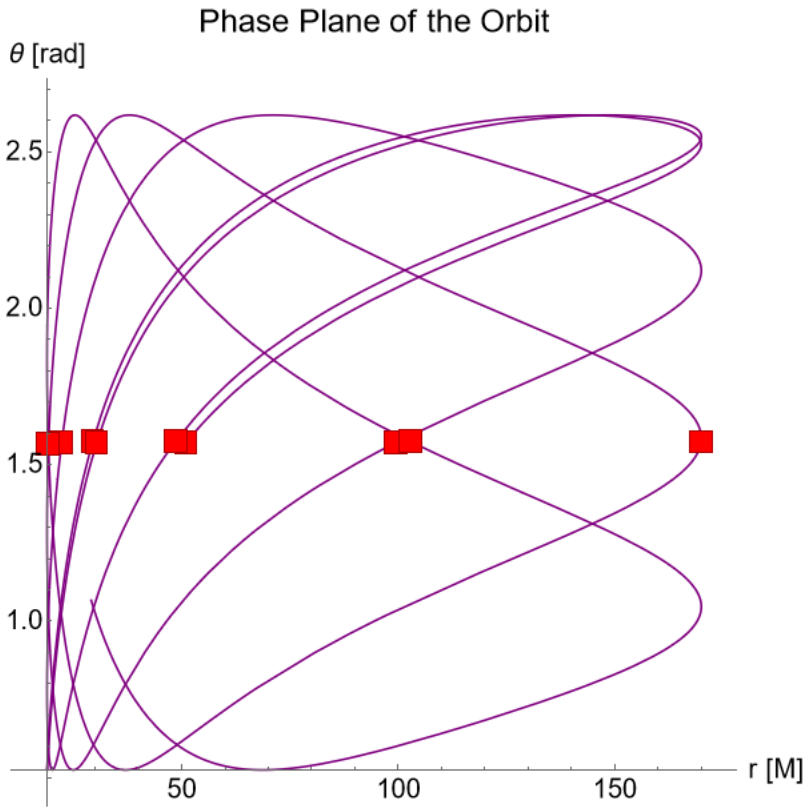

Figure 11: The phase plane of the optimum solution, with outbursts marked as red dots.

the outburst maxima, allowing a better comparison with observation and more insight into the exact nature of the OJ 287 system.

Possibly the largest limitation of the analysis presented in this investigation is the lack of resolution from the scan over parameter space and the difficulty of performing an accurate error analysis. Using the aforementioned grid method to scan over parameter space is straightforward and converges to a result, however it is computationally inefficient which restricts the resolution of the grid and naturally reduces the accuracy of the scan. Furthermore, in order to perform a scan over the parameter space at the one time, the ranges of the parameters must be chosen which produce physically realisable orbits for all parameter combinations, which means that orbits for some physically realistic parameter combinations are not being accounted for because at least one of the parameters are not physically realisable for another combination of parameters. This limits the ranges that can be used for the brute force scanning.

Due to the computational cost of the parameter scanning, the step size for each parameter must be chosen carefully in order to scan finely enough while still evaluating in a reasonable time. However, parameter combinations which lie in between the grid points are naturally not accounted for, and a loss of resolution occurs due to this. As a first approximation in the error analysis could be to take the grid spacing for each parameter as the error on that parameter. Although since reducing the grid size for one parameter introduces a range of other parameter combinations for the other parameters,

error propagation must be taken into account, which complicates the error analysis. The error from observations must also be taken into account.

A more thorough and reliable method could be to use random walks within parameter space to converge to the correct result. Bayesian statistics could provide a way to provide a confidence interval of the obtained values by considering the priors and posteriors, where a prior probability describes the original beliefs of the system and the posteriors describe the new information gained during the parameter estimation. There are ongoing efforts to analyse the OJ 287 system, and blazars in general, with Bayesian statistics, which could offer statistical analysis of more desirable precision and accuracy [23].

7 Conclusion

We successfully analysed the supermassive binary black hole system OJ 287 in this investigation. We implemented the Kerr geodesic equations numerically, which we used to calculate orbital intersection points with the $\theta = \pi/2$ plane, assumed the be the plane of the accretion disk, upon which an interaction with the orbiting secondary black hole would cause a burst in light intensity. We scanned through parameter space using the grid scanning method. We found the extracted optimal parameter solutions for the OJ 287 system to be $M = 3 \times 10^{10}\,\mathrm{M}_\odot$, $a = 0.1$, $p = 34$, $e = 0.8$ and $\theta_{\min} = \pi/6$, where a and p are in geometrised units of the black hole mass, leading to a semi-latus rectum size of approximately $10,070$ Au. We calculated the predicted outburst times which are given in Table 6 with the average magnitude of the outburst time discrepancy as 8.64 years, leading to a moderate fit with observations. The main causes of discrepancies between the calculations are observations are the approximation of the trajectory as a geodesic and the parameter scanning method, in which resolution is lost due to the clipping and the coarse discretisation of the parameter scanning ranges. We recommend a mass ratio expansion for the orbital trajectory and an alternative parameter scanning method, such as random walks with Bayesian statistical analysis, in order to improve the model and the analysis.

8 Appendix

8.1 Constants of Motion in Kerr Space-Time

The geodesic equations were derived in terms of the parameters (E, L_z, Q), however, Schmidt derived the relationship between these constants and the more convenient $(p, e, \theta_{\min})$ [21].

We can relate the dimensionful quantities to their dimensionless counterparts with $E = \mu\tilde{E}$, $L_z = \mu M\tilde{L}_z$ and $Q = (\mu M)^2\tilde{Q}$. Given a minimum orbital radius r_1 and a maximum radius r_2, where $r_1 = p/(1+e)$ and $r_2 = p/(1-e)$, we can relate the constants with the following equations. Note that $D = \mathrm{sgn}L_z$ and specifies whether the orbit is prograde or retrograde, given $D = +1$ or $D = -1$ respectively.

$$\tilde{E}^2 = \frac{\kappa\rho + 2\epsilon\sigma - 2D\sqrt{\sigma(\sigma\epsilon^2 + \rho\epsilon\kappa - \eta\kappa^2)}}{\rho^2 + 4\eta\sigma}\,, \tag{49}$$

$$\tilde{L}_z = -\frac{g_1\tilde{E}}{h_1} + D\sqrt{\frac{g_1^2\tilde{E}^2}{h_1^2} + \frac{f_1\tilde{E}^2 - d_1}{h_1}}\,, \tag{50}$$

$$\tilde{Q} = z_-\left(\beta + \frac{\tilde{L}_z^2}{1-z_-}\right)\,, \tag{51}$$

where we define $\tilde{a} = a/M$, $z_- = \cos^2\theta_{\min}$ and $\beta = \tilde{a}^2(1-\tilde{E}^2)$, with the functions

$$\tilde{\Delta}(\tilde{r}) = \tilde{r}^2 - 2\tilde{r}^+\tilde{a}^2\,, \tag{52}$$

$$d(\tilde{r}) = \tilde{\Delta}(\tilde{r}^2 + z_-\tilde{a}^2)\,, \tag{53}$$

$$f(\tilde{r}) = \tilde{r}^4 + \tilde{a}^2(\tilde{r}(\tilde{r}+2) + z_-\tilde{\Delta})\,, \tag{54}$$

$$g(\tilde{r}) = 2\tilde{a}\tilde{r}\,, \tag{55}$$

$$h(\tilde{r}) = \tilde{r}(\tilde{r}-2) + \frac{z_-\tilde{\Delta}}{1-z_-}\,, \tag{56}$$

and the determinants

$$\kappa = d_1h_1 - d_2h_1\,, \tag{57}$$

$$\epsilon = d_1g_2 - d_2g_1\,, \tag{58}$$

$$\rho = f_1h_2 - f_2h_1\,, \tag{59}$$

$$\eta = f_1g_2 - f_2g_1\,, \tag{60}$$

$$\sigma = g_1h_2 - g_2h_1\,. \tag{61}$$

A subscript 1 or 2 means that the function should be evaluated at the dimensionless radius $\tilde{r}_{1,2}$.

9 References

[1] Lankeswar Dey, Achamveedu Gopakumar, Mauri Valtonen, Stanislaw Zola, Abhimanyu Susobhanan, Rene Hudec, Pauli Pihajoki, Tapio Pursimo, Andrei Berdyugin, Vilppu Piirola, et al. The unique blazar OJ 287 and its massive binary black hole central engine. *Universe*, 5(5):108, 2019.

[2] Seppo Laine, Lankeswar Dey, Mauri Valtonen, A Gopakumar, Stanislaw Zola, S Komossa, Mark Kidger, Pauli Pihajoki, José L Gómez, Daniel Caton, et al. Spitzer observations of the predicted eddington flare from blazar oj 287. *The Astrophysical Journal Letters*, 894(1):L1, 2020.

[3] M. L. Sitko and V. T. Junkkarinen. Continuum and line fluxes of OJ 287 at minimum light. *Publications of the Astronomical Society of the Pacific*, 97(598):1158, 1985.

[4] Lankeswar Dey, MJ Valtonen, A Gopakumar, S Zola, R Hudec, P Pihajoki, S Ciprini, K Matsumoto, K Sadakane, M Kidger, et al. Authenticating the presence of a relativistic massive black hole binary in OJ 287 using its general relativity centenary flare: Improved orbital parameters. *The Astrophysical Journal*, 866(1):11, 2018.

[5] J. I. Katz. A precessing disk in OJ 287? *The Astrophysical Journal*, 478(2):527, 1997.

[6] Martin J Rees. Black hole models for active galactic nuclei. *Annual review of astronomy and astrophysics*, 22(1):471–506, 1984.

[7] Harry J Lehto and Mauri J Valtonen. OJ 287 outburst structure and a binary black hole model. *The Astrophysical Journal*, 460:207, 1996.

[8] B Kapanadze, D Dorner, STEFANO Vercellone, Patrizia Romano, P Hughes, M Aller, H Aller, M Reynolds, and L Tabagari. Strong x-ray and multiwavelength flaring activity for 1es 1959+ 650, 2016 august–2017 november. *The Astrophysical Journal Supplement Series*, 238(1):13, 2018.

[9] S Komossa, D Grupe, ML Parker, MJ Valtonen, JL Gómez, A Gopakumar, and L Dey. The 2020 april–june super-outburst of OJ 287 and its long-term multiwavelength light curve with swift: binary supermassive black hole and jet activity. *Monthly Notices of the Royal Astronomical Society: Letters*, 498(1):L35–L39, 2020.

[10] John Kormendy and Douglas Richstone. Inward bound—the search for supermassive black holes in galactic nuclei. *Annual Review of Astronomy and Astrophysics*, 33(1):581–624, 1995.

[11] John Candee Dean. The story of halley's comet. *Popular Astronomy*, 16:331–345, 1908.

[12] JG Galle. Account of the discovery of le verrier's planet neptune, at berlin, sept. 23, 1846. *Monthly Notices of the Royal Astronomical Society*, 7:153, 1846.

[13] Michael Paul Hobson, George P Efstathiou, and Anthony N Lasenby. *General relativity: an introduction for physicists*. Cambridge University Press, 2006.

[14] Charles W Misner, Kip S Thorne, and John Archibald Wheeler. *Gravitation*. Macmillan, 1973.

[15] Ezra Newman, L Tamburino, and Theodore Unti. Empty-space generalization of the schwarzschild metric. *Journal of Mathematical Physics*, 4(7):915–923, 1963.

[16] Karl Schwarzschild. Über das gravitationsfeld einer kugel aus inkompressibler flüssigkeit nach der einsteinschen theorie. *Sitzungsberichte der königlich preußischen Akademie der Wissenschaften zu Berlin*, pages 424–434, 1916.

[17] Roy P Kerr. Gravitational field of a spinning mass as an example of algebraically special metrics. *Physical review letters*, 11(5):237, 1963.

[18] Brandon Carter. Global structure of the kerr family of gravitational fields. *Physical Review*, 174(5):1559, 1968.

[19] Steve Drasco and Scott A Hughes. Gravitational wave snapshots of generic extreme mass ratio inspirals. *Physical Review D*, 73(2):024027, 2006.

[20] Yasushi Mino. Perturbative approach to an orbital evolution around a supermassive black hole. *Physical Review D*, 67(8):084027, 2003.

[21] Wolfram Schmidt. Celestial mechanics in kerr spacetime. *Classical and Quantum Gravity*, 19(10):2743, 2002.

[22] Andrew Robinson. Did Einstein really say that? *Nature*, 557(7703):30–31, 2018.

[23] Makoto Uemura, Koji S Kawabata, Mahito Sasada, Yuki Ikejiri, Kiyoshi Sakimoto, Ryosuke Itoh, Masayuki Yamanaka, Takashi Ohsugi, Shuji Sato, and Masaru Kino. Bayesian approach to find a long-term trend in erratic polarization variations observed in blazars. *Publications of the Astronomical Society of Japan*, 62(1):69–80, 2010.